Journal of
Materials Chemistry A

Materials for energy and sustainability

Accepted Manuscript

Journal of
Materials Chemistry A

Materials for energy and sustainability

rsc.li/materials-a

Volume 6
Number 12
28 March 2018
Pages 4883–5230

ISSN 2050-7488

COMMUNICATION
Zhenhai Wen et al.
An electrochemically neutralized energy-assisted low-cost acid-alkaline electrolyzer for energy-saving electrolysis hydrogen generation

ROYAL SOCIETY
OF CHEMISTRY

ROYAL SOCIETY
OF **CHEMISTRY**

rsc.li/materials-a

Two-step MAPbI₃ deposition by Low-Vacuum Proximity-Space-Effusion for high-efficiency inverted semitransparent perovskite solar cells

Emanuele Smecca,[a] Vitantonio Valenzano,[b] Salvatore Valastro,[a,c] Ioannis Deretzis,[a] Giovanni Mannino,[a] Graziella Malandrino,[d] Gianluca Accorsi,[e] Silvia Colella,[f] Aurora Rizzo,[e] Antonino La Magna,[a] Andrea Listorti,*[e,g] Alessandra Alberti*[a]

a CNR-IMM Zona industriale, Strada VIII 5, 95121, Catania, Italy
b Dipartimento di Matematica e Fisica "E. De Giorgi", Università del Salento, Campus Ecotekne, Via Arnesano, 73100 Lecce, Italy
c Dipartimento di Fisica e Astronomia, Università di Catania, Via S. Sofia 64, 95123 Catania, Italy
d Dipartimento di Scienze Chimiche. Università degli Studi di Catania. V.le A. Doria 95125 Catania. Italy
e CNR NANOTEC, Institute of Nanotechnology, c/o Campus Ecotekne, via Monteroni, 73100 Lecce, Italy
f CNRNANOTEC, Institute of Nanotechnology, c/o Department of Chemistry, University of Bari 'Aldo Moro', via Orabona 4, 70126 Bari, Italy
g Department of Chemistry, University of Bari "Aldo Moro", via Orabona 4, 70126, Bari, Italy
*corresponding author
Email:alessandra.alberti@imm.cnr.it; andrea.listorti@uniba.it

Abstract

Halide perovskite solar cells can combine high photoconversion efficiency with high transmittance. Herein, we developed an innovative vacuum deposition method to prepare CH₃NH₃PbI₃ (MAPbI₃) thin film for semitransparent perovskite solar cells. The method applies a two steps Low-Vacuum Proximity-Space-Effusion (LV-PSE) under low vacuum conditions to produce high-quality thin layers of phase-pure MAPbI₃. The parameter optimization was validated by theoretical calculation. We show that, during the process of CH₃NH₃I (MAI) deposition (second step) on PbI₂ (first step) at a given substrate temperature, the conversion of the PbI₂ film to MAPbI₃ occurs from the top-surface inward via an adsorption-incorporation-migration mechanism guided by the gradient of MAI concentration. The quality of the final layer arises from this progressive conversion that exploits the lattice order of the mother PbI₂ layer. Finally, p-i-n solar cells were prepared using ITO/PTAA/MAPbI₃/PCBM-BCP/Al architectures with photo-active layer thickness of 150nm. This layer, characterized by an Average Visible Transmittance (AVT) as high as 20%, produced an average efficiency of 14.4% that is a remarkable result considering the transparency vs. efficiency countertrend that indeed demands a proper balance from the quality of the material.

Very importantly, we demonstrated that further down scalability of the MAPbI₃ layer is feasible as proved by reducing the thickness down to 80 nm. In this specific case, the devices showed an average efficiency of 12.9% withstanding an AVT of 32.8%. This notable efficiency recorded on those extremely thin layers benefits from the exclusive quality of the MAPbI₃ grown with the developed method.

1. Introduction

Hybrid Organic-Inorganic Perovskites are worldwide one of the most investigated materials today, due to their unique properties impacting various fields as Photovoltaics,[1-4] Light Emission Devices(LEDs)[5,6] and Photodetectors.[7-9] In PV, thanks to the wide absorption range and excellent charge carrier lifetime and diffusion[10] of the material, Perovskite Solar Cells (PSCs) were able to reach the exceptional goal of 25.5%[11] just ten years after the first publication of Miyasaka *et al.* [12] in 2009. All their exceptional properties, deriving from the possibility of preparing high quality films in terms of crystallinity, thickness and low defect density, are strictly related.[13-15] Counterbalancing these advantages, there are still issues related to the device stability particularly in humid air ambient[16,17], and to the realization of high-quality large area films via wet deposition approaches, which cool down their attractiveness from the industrial point of view. A great effort was dedicated improving the stability[18,19] and crystallinity[20] of the perovskite polycrystalline films, but most of the work was focused on spin coating or solvent dependent technologies.

In this perspective, although vacuum deposition methods are more suitable in terms of industrial throughput, they were less investigated, despite some seminal work[21-24] demonstrating how hybrid organic inorganic perovskite films prepared by co-evaporation possess higher stability and performances with respect films prepared by spin coating techniques. In this context, a record efficiency of 20.8% was achieved using high vacuum conditions, (~1x10^{-6} mbar) by Perez del Rey *et al.*[25] with a co-evaporation of MAI and PbI$_2$ for a 590 nm-thick layer of MAPbI$_3$. More recently, Arivazhgan et al.[26] have studied in detail the role of vapor pressure in a range of high-vacuum (HV) conditions between 5.6x10^{-5} Torr and 5.6x10^{-6} Torr finding the best condition at 3.3x10^{-5} Torr that allowed a 350-thick MAPbI$_3$ layer achieving 15.74% cell efficiency Guo et al. [27] used the well-known closed space sublimation (CSS) technique for deposition of organic materials to convert a pristine spin-coated PbI$_2$ into MAPI by sublimation of MAI powders at a short distance (~1 mm). They obtained a best efficiency of 16.2% with a 4 mm^2 active area device. Gu et al.[28] exploited the same technique but depositing 820 nm thick films of mixed lead halide perovskite, thus achieving a remarkable 20.44% efficiency on a 0.07 cm^2 active solar cell area. Nonetheless, in CSS the limitation of a solution processing step for the deposition of PbI$_2$ still remains. Another approach was proposed by Ng et al.[29] consisting of a deposition of a multilayered stack of PbI$_2$ and MAI with a post annealing treatment to form the MAPbI$_3$ film. With this technique they were able to reach a 11.4% using 473nm thick MAPbI$_3$ layers. Useful insights can be found in the paper by Baekbo *et al.*[30] wherein the role of the MAI vapor pressure is highlighted as pivotal to overcome the limitation of the low

stitching coefficient into the substrate due to re-desorption of the evaporated species. This issue indeed poses the need of a different design of the PVD chamber.

Together with the lack of solvent, another advantage of MAPbI$_3$ purely deposited by physical methods is the very low roughness and the possibility to scale down the thickness of the active layer maintaining uniformity and compactness. As a major consequence, the content of Pb in the devices would be reduced if thin MAPbI$_3$ layers were applied with sufficiently high photon-to-electron conversion efficiency. As a further main impact of the thickness scaling, the augmented transparency of MAPbI$_3$ in the visible range opens the possibility to produce semitransparent solar cells for BIPV.[31-38] Reducing the thickness would finally impact on the production costs. In this respect, in their life cycle analyses Li *et al.* [39] asserted that the cost of PbI$_2$ is one of the most critical for Si/PSC tandem solar cells. To our knowledge, the best efficiency reached with a semitransparent perovskite coupled with a CIGS bottom cell device is 18.1% by Sheng *et al.*[40] using a quadruple cations active layer in a standard n-i-p architecture deposited by spin coating technique as top cell. In a very recent work, a 18.4% efficiency was achieved by Xu *et al*[41] with a triple halide perovskite layer as top cell for tandem technology boosted at 27.1% when coupled with a bottom Si solar cell. In both cases however, the semitransparent perovskite solar cells have been produced by solution process techniques that, generally speaking, offer low industrial throughput or undesired contaminations (i.e. residual solvents) or incompatible thermal processes.

One of the first works on vacuum evaporation deposition of semitransparent perovskite films was done by Ono et al.[42] wherein, by a co-deposition of PbCl$_2$ and MAI in a home-built instrumentation, an efficiency of 9.9% was reached with a 5 cm x 5 cm sample, attesting the industrial potential of the vacuum deposition technique. In that work, a good crystal quality of the film was assured controlling the vapor pressure of MAI inside the chamber at $\approx 2 \times 10^{-3}$ mbar during the co-evaporation.

In our work, we have prepared MAPbI$_3$ layers by a fully solvent free process using a customized deposition chamber. The method consists of two-step Proximity-Space-Effusion of species under Low-Vacuum conditions (LV-PSE) wherein the substrate is posed at medium range distance with respect to the sources. The method is characterized by the low vacuum in the deposition chamber and the short diffusion path of the sublimated species that tailor a condition of high pressure and high temperature of the species reaching the substrate side. This combination upsets different kinetic properties of the species impinging on the substrate with respect to standard HV-PVD (high vacuum physical vacuum deposition) with a major impact on the material quality. As a further effect,

the number of the available sensible parameters is increased by 2. We, in fact, demonstrate that in LV-PSE processes, chamber pressure and source-substrate distance become additional parameters to rise the quality of the perovskite with the intent of downscaling of the perovskite thickness without excessively penalizing the photovoltaic performances. In addition, the method is intrinsically low-cost and at quasi-zero loss of material at the chamber walls to restrain investment and operation costs. The deposited layers were characterized in terms of structure and morphology and optical properties. Finally, solar cells with p-i-n architecture composed by ITO / polytriarylamine (PTAA) / MAPbI$_3$ / Phenyl-C61-butyric acid methyl ester (PCBM) / Al were prepared and tested, resulting in competing performances for perovskite layers in the range 80-150 nm.

This newly conceived process opens new perspective for the benefit of the industrial throughput and for the development of semitransparent perovskite solar cells to be applied in BIPV as well as on flexible PV.

2. Experimental

Materials

The MAPbI$_3$ films were deposited with a specifically customized[43] vacuum deposition equipment provided by Kenosistec s.r.l and with a newly conceived low-vacuum proximity-space-effusion (LV-PSE) method. For the precursor materials, lead iodide powders (99.99% purity) were purchased from Sigma Aldrich. Methyl Ammonium Iodide was purchased by Dyenamo AB. All materials were used as received without any further purification. Thermal indicator were purchased form RS Components S.r.l.

Device preparation

Photovoltaic devices have a final structure ITO/PTAA/MAPbI3/PCBM/BCP/Al, where ITO is indium tin oxide and PTAA is poly(bis(4-phenyl)(2,5,6-trimethylphenyl)amine), a conventional hole transport layer (HTL).

ITO-coated glass substrates (4L patterned) were rinsed with Milli-Q water and then cleaned by 10 min of sonication in two steps with acetone, followed by isopropanol. The PTAA layer was deposited onto the substrate by spin coating technique at 6000 r.p.m. for 30 s, starting from 1.5 mg/mL toluene solution. Then, the perovskite layer was deposited onto PTAA by a two steps Low-Vacuum Proximity-Space-Effusion (LV-PSE) under low vacuum condition. Subsequently, the PCBM electron-transport layer (ETL) was deposited by 25 mg/ml chlorobenzene solution. The solution was filtered
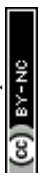
with a hydrophobic 0.20 μm PTFE filter and then spin coated onto MAPI layer at 1000 r.p.m. for 60 s. Then, an ultrathin layer of bathocuproine (BCP) with high electron affinity was spin coated on the top of PCBM. Finally, Al metal electrode of about 100 nm was thermally evaporated at a pressure of 4×10^{-6} mbar on top of the HTM layer to form the back contact. All the processes after the deposition of MAPI layer were carried out inside a glovebox with oxygen and water levels below 1 ppm and a temperature strictly between 20 and 25 °C.

Material characterization

XRD patterns were collected by using a D8Discoved (Bruker AXS) diffractometer equipped with a high precision goniometer (0.0001 Å), a thin film attachment (long soller slits) and a Cu-Ka source. Morphological analyses were performed using a field emission scanning electron microscope Zeiss SUPRA 55 VP with a field emission electron gun. The XPS spectra were performed with a PHI ESCA/SAM 5600 Multi technique spectrometer equipped with Mg standard Kα X-ray source. Binding Energy scale was calibrated by centering the adventitious/hydrocarbon carbon C 1s at 285.0 eV. A. J.A. Woollam VASE ellipsometer equipped with monochromator and autoretarder was used to measure the changes in the optical constants. Steady state and time resolved photoluminescence were measured by an Edinburgh FLS980 spectrometer equipped with a Peltier- cooled Hamamatsu R928 photomultiplier tube (185-850 nm). An Edinburgh Xe900 450 W Xenon arc lamp was used as exciting light source. Corrected spectra were obtained via a calibration curve supplied with the instrument (lamp power in the steady state PL experiments 0.6 mW cm-2, spot area 0.5 cm2). Emission decay time were determined with the single photon counting technique by means of the same Edinburgh FLS980 spectrometer using a laser diode as excitation source (1 MHz, exc = 405 nm, 67 ps pulse width and about 20 ps time resolution after deconvolution) and a Hamamatsu MCP R3809U-50 (time resolution 20 ps) as detector. (Laser power in the TRPL experiment 1.6 Wcm-2, spot area 0.3 mm2).44

Theoretical calculations

Calculations were performed within the Density Functional Theory (DFT), using the plane-wave Quantum Espresso code.[45] The Perdew-Burke-Ezernhof implementation[46] of the generalized gradient approximation was used for the description of the exchange-correlation functional, along with ultrasoft pseudopotentials.[47] Models considered the initial stages of $MAPbI_3$ formation through the consecutive intercalation of MA^+/I^- ions within $3 \times 3 \times 2$ hexagonal PbI_2 supercells. The calculation

cutoff for the kinetic energy and the augmented charge density were set to 46 Ry and 326 Ry, respectively. A 2×2×2 Monkhorst-Pack grid[48] was used for the sampling of the Brillouin zone. Both atoms and lattice parameters were allowed to fully relax.

Device electrical characterization

The devices were characterized using a Keithley 2400 Source Measure Unit and AirMass 1.5 Global (AM 1.5G) solar simulator (Newport 91160A) with an irradiation intensity of 100 mW/cm². The solar simulator irradiance was set to 100 mW cm^{-2} using a thermopile radiant power meter with fused-silica window (Spectra 3 Physics Oriel, model 70260). The planar dimension of the active area in a complete device was measured with full precision using a microscope. All devices were tested using 100 mV/s or 1000 mV/s scan rates, under nitrogen at 20 to 25 °C.

3. Results and discussion

Deposition process

The MAPbI$_3$ layers were deposited under low vacuum conditions by a two-step method based on Proximity-Space-Effusion (LV-PSE) of species from Knudsen cells with exit orifice having tunable size. The growth method represents a novelty in the field and indeed it is illustrated in figure 1 and in detail along the text of the paper. We in particular highlight the compactness of the equipment and the use of low-vacuum in the deposition chamber. The first condition arises from the extremely reduced source-substrate distance that can be efficiently modulated in the range 1-3 cm. The use of low-vacuum, on one hand, represents a huge advantage for the initial cost and maintenance of the equipment; on the other hand it allows using the chamber pressure as an additional process parameter to create an exit flux of species at high energy and density. In standard HV-PVD, instead, the source-substrate distance is several tens of centimeters and high vacuum conditions are applied. This implies that the impinging flux on the substrate has a high temperature (T) and low vapour pressure (P) in HV-PVD while in LV-PSE the temperature (T) is still high and the vapour pressure (P) is also hgh for the benefit of the material quality.[30] The comparison is sketched in figure 1.

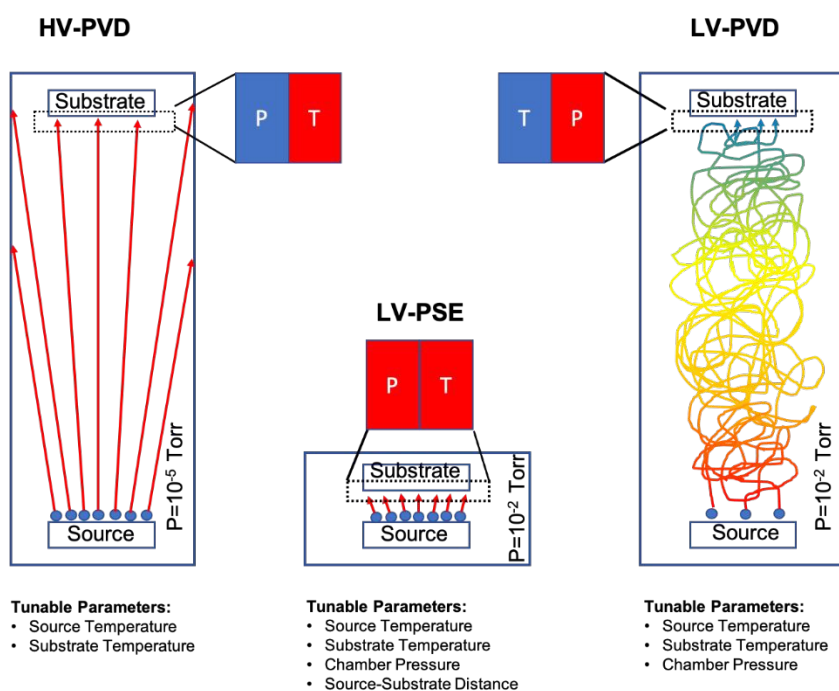Journal of Materials Chemistry A Accepted Manuscript

Figure 1 : Schematic of three physical deposition methods. The HV-PVD applied in the current literature works at high vacuum (e.g. 10^{-5} Torr) and with long diffusion path such that in the substrate proximity low pressure and high temperature of the sublimated species are established. On the contrary, our LV-PSE method is characterized by low vacuum and short diffusion path that tailor high pressure and high temperature of adatoms at the substrate side. This combination upsets the kinetic properties of the species impinging on the substrate with a major impact on the material quality and with a further effect on increasing the number of the available operation (tunable) parameters. Lastly, the right panel illustrates how moving from LV-PSE to LV-PVD (i.e. setting the source-substrate distance as in the HV-PVD) implies a drastic reduction of the kinetic energy of the adatoms (temperature) at the substrate that comes from the collisional path at low vacuum and indeed makes unfeasible any deposition in a reasonable timescale

The LV-SPE method is indeed mid-way between conventional high-vacuum thermal evaporation[25,30] and close-space-sublimation[27] bearing some advantages from both sides. It operatively works as a sequential deposition of the inorganic layer (PbI_2) followed by the evaporation of the organic moieties (MAI) that progressively infiltrate into it (figure 2a). No further thermal treatments are needed after deposition, and this represents a value-added to reduce processing times and costs. The mainstay resides in the substrate coaxially placed over the source at an optimized medium distance from the orifice ~2 cm (1-3 cm) that moves over each source on purpose. This short distance between the source and the substrate allows the molecules of the organic halide to arrive at the top of PbI_2 film with enough energy to start the conversion reaction. Conversion reaction would be unfeasible with the substrate positioned at the typical distance of HV-PVD (see figure 1). This short distance enable the use of low vacuum conditions in the chamber (i.e. ~4×10^{-2} mbar) that reduces the process complexity and costs. Moreover, with proper implementation of the equipment, the chamber pressure can easily become a further parameter, together with the source temperature, to tune the energy of the gas species from the source Conversely, under low vacuum conditions, enlarging the source-substrate distances to tens of centimeters causes collisional paths within the gas during travelling that produce huge energy loss of the sublimated species before their

arrival at the substrate surface with abundant material accumulation at the chamber walls. Collisions, enormously reduce deposition rate and increase contamination incorporation into the layer. At high vacuum condition and high source-substrate distances as in HV-PVD (figure 1), instead, the gas molecules would retain their energy until their arrival at the substrate but with lower vapour pressure at the substrate surface due to a geometrical effect (spread of the flux along long distances). As instead pointed out in ref Baekbo *et al,*[30] high MAI vapour pressure is needed to overcome the limitation of the low stitching coefficient.

Therefore, with LV-PSE it is possible to use low vacuum condition while retaining high gas molecules energy on the substrate, maintaining a good deposition rate and, at the same time, reducing the loss of the sublimated species on the chamber sidewall. Hsiao et al.[49] investigated the role of chamber pressure but in a range that does not cover the one we used. As a first observation, they investigated between 10^{-5} Torr and 10^{-3} Torr (our working condition is around $2\text{-}4\times10^{-2}$ Torr). Most importantly, they attributed to the pressure increase a negative valence as the best efficiency was there obtained by applying 10^{-4} Torr with a reported solar cell efficiency of 17.6% with 480 nm of perovskite This result introduces the importance of a proper combination of low-vacuum with short source-substrate distances to get competitive efficiencies at low perovskite thicknesses, as we did with our method.

An evaluation of the LV-PSE process in term of material growth is provided from the estimates of the mass transfer rate from the Knudsen cells and the substrate. The mass effusion rate from the cell's orifice can be calculated form the partial pressure of the molecular gas in the cell, which i.e. for the PbI_2 case is reported in Kendler et al.[50]

$$\frac{dm}{dt} = A_0\left(1 + 3\frac{l_0}{4d_0}\right)^{-1} \times \sqrt{\frac{1}{2\pi RTM_{PbI2}}}(p_v - p_{chamb}) = A_0\left(1 + 3\frac{l_0}{4d_0}\right)^{-1} \times \sqrt{\frac{1}{2\pi RTM_{PbI2}}}$$
$$\left\{exp\left[-\frac{H_{PbI2}}{R}\left(\frac{1}{T} - \frac{1}{T_{PbI2}}\right)\right] - p_{chamb}\right\} \qquad\qquad \text{eq 1}$$

where T is the cell temperature p_{chamb} the chamber pressure outside the cell; M_{PbI2} H_{PbI2} and T_{PbI2} are the PbI_2 molar mass, sublimation enthalpy and sublimation temperature respectively; while A_0 d_0 and l_0 are the orifice area, diameter and thickness respectively. Analogous expression could be also used for the MAI molecular gas with the proper material dependent parameter.

Assuming that quasi-ballistic transport conditions occur for the molecules transport from the cell's orifice to the substrate, an approximate estimate of the growth rate for the PbI_2 in the central
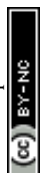
position of the substrate (in a symmetric configuration) can be obtained from the balance between the deposition flux (J_{dep}) and the evaporation flux (J_{ev})using the formula by Avrov et al.[51]

$$Gr = \frac{M_{PbI2}}{\varrho_{PbI2}}(j_{dep} - j_{ev}) = \frac{M_{PbI2}}{\rho_{PbI2}}\left(\frac{1}{\pi r_0^2}\frac{dm}{dt} - j_{ev}\right) \quad \text{eq 2}$$

where ρ_{PbI2} is the PbI$_2$ density, r_0 is the distance between the orifice and the substrate center. The deposition flux can be calculated from the mass effusion rate while for j_{ev} we use the equation:

$$j_{ev} = \sqrt{\frac{1}{2\pi RT_{film}M_{PbI2}}}exp\left[-\frac{H'_{PbI2}}{R}\left(\frac{1}{T_{film}} - \frac{1}{T_{PbI2}}\right)\right] \quad \text{eq 3}$$

where a different value of the enthalpy is considered for the local evaporation/desorption from the growing film at the temperature T_{film} .

In figure 2b a comparison between the PbI$_2$ growth rate prediction, using the above equations, and the measured growth rate at three different distances between the cell and the substrate is shown. The substrate temperature values have been also measured using thermal indicator strips chosen in the appropriate range. The values are $T_{film} = 150, 120, 100\,°C$ for $r_0 = 1, 2 \text{ and } 3\,cm$ respectively. The chamber pressure is $p_{chamb} = 0.04\,mbar$. Both the model and the experimental data agree that the Knudsen cell's temperature at which deposition can be observed is T>350°C. Moreover, the experimental and theoretical optimal value for the growth rate is obtained for the couple parameters T_{film} 120 °C and $r_0 = 2\,cm$.

In this analysis we use the literature Chickos et al[52] and Dualeh et al.[53] and the derived values H$_{PbI2}$ $= 163.1\frac{kJ}{mol}$ and $T_{PbI2} = 646\,K$ while the $H'_{T_{PbI2}} = 127\frac{kJ}{mol}$ has been used for the evaporation/desorption flux. A lower value of the enthalpy constant (which can be considered a fitting parameter of the model) for the evaporation considers that the competitive process with respect to the deposition involves the PbI$_2$ molecules absorbed at the film surface which are on average less strongly bound with respect the ones present in the materials loaded in the Knudsen cell.

With our optimized process conditions, the deposition rate for the PbI$_2$ is around 3 nm/min while about 60 minutes are needed to complete the conversion of the PbI$_2$ into MAPbI$_3$ having a final desired thickness of 150 nm. The temperature for PbI$_2$ sublimation was set at 350 °C. For the MAI deposition step, a temperature of 135 °C was used and the deposition time was optimized to reach the right stoichiometry and to avoid any presence of residual PbI$_2$ on the sample. Immediately after the MAI deposition, the chamber is filled with N$_2$ to avoid decomposition of the MAPbI$_3$ layer due to vacuum.[16,54,55] The substrate temperature during the MAI deposition is 75 °C. That settles the
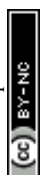
best conditions for MAPbI$_3$ formation. Accordingly, this temperature is given in literature[30,49] as the best one for MAPbI$_3$ conversion via two-step deposition processes.

With this procedure we deposited thin layers of MAPbI$_3$ with thickness 150 nm and 80 nm, to demonstrate that a significant down-scaling is feasible with the LV-PSE method.
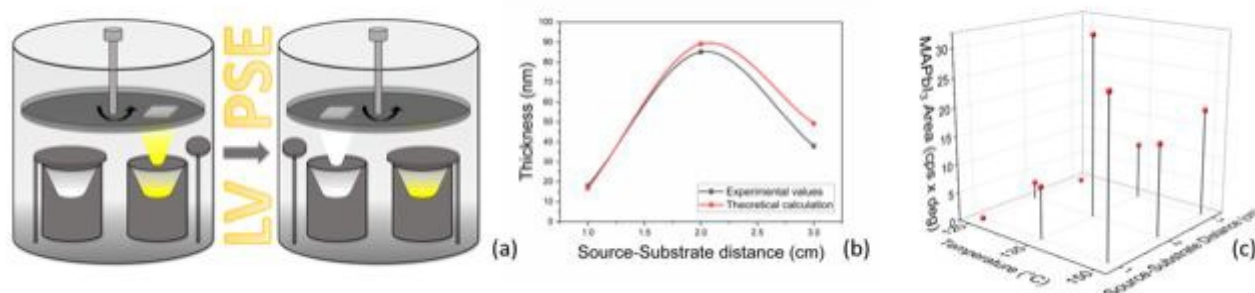

Figure 2 (a) Schematic representation of the low-vacuum deposition chamber for the two-step Low-Vacuum Proximity-Space-Effusion (LV-PSE) process used for the preparation of MAPbI$_3$. (b) Comparison between the thickness of PbI$_2$ layer deposited in 30 minutes at different source-substrate distances and theoretical values obtained through the model.(c) Optimization of the MAI temperature and source-substrate distance obtained by the XRD analyses for the MAI deposition step. We reported the area of the peak at 2θ=14.1° for all the combination used.

The optimization on temperature of the crucible and source-substrate distance for MAI deposition step is shown in figure 2c where we plot the area of the XRD peak of the MAPbI$_3$ peak at 2θ=14.1° for all the combination of investigated temperatures and source-substrate distances. The best combination pf parameters was 135 °C with a distance of 2 cm, that we consistently used for the preparation of the devices. In this case in fact, we obtained the highest area for the MAPbI$_3$ peak and no peak was detected for PbI$_2$. Even though a good result was also obtained using 150 °C at distance of 1 cm, we decided to use the previous combination for the lower working temperature of the crucible, to longer preserve the MAI powder, and for a lower production energy consumption that is one of the main prerogatives of our technique. For the substrate temperature, we found, by means of direct temperature measurements, that the proximity between the source and substrate causes a self-heating of the substrate that must be taken into account. The overall balance between self-heating and cooling provides a final temperature of 75 °C for the combination of temperature and distance of 135 °C 2cm. This is well known to be the convenient temperature for MAI reaction.[30,49]

Figure 3a shows the XRD patterns collected on 150 nm and 80 nm films deposited on ITO/PTAA substrates. In both samples we observe the diagnostic peaks related to MAPbI$_3$ centered at

2θ=14.1°, 28.4° and 35.2°. The lack of the peak at 12.67° related to PbI$_2$ excludes the presence of residual PbI$_2$ inside the films. Considering that the two samples have the same size, the intensities of homogeneous peaks can be compared and suggests that the 150 nm-thick film has a high crystallographic quality.
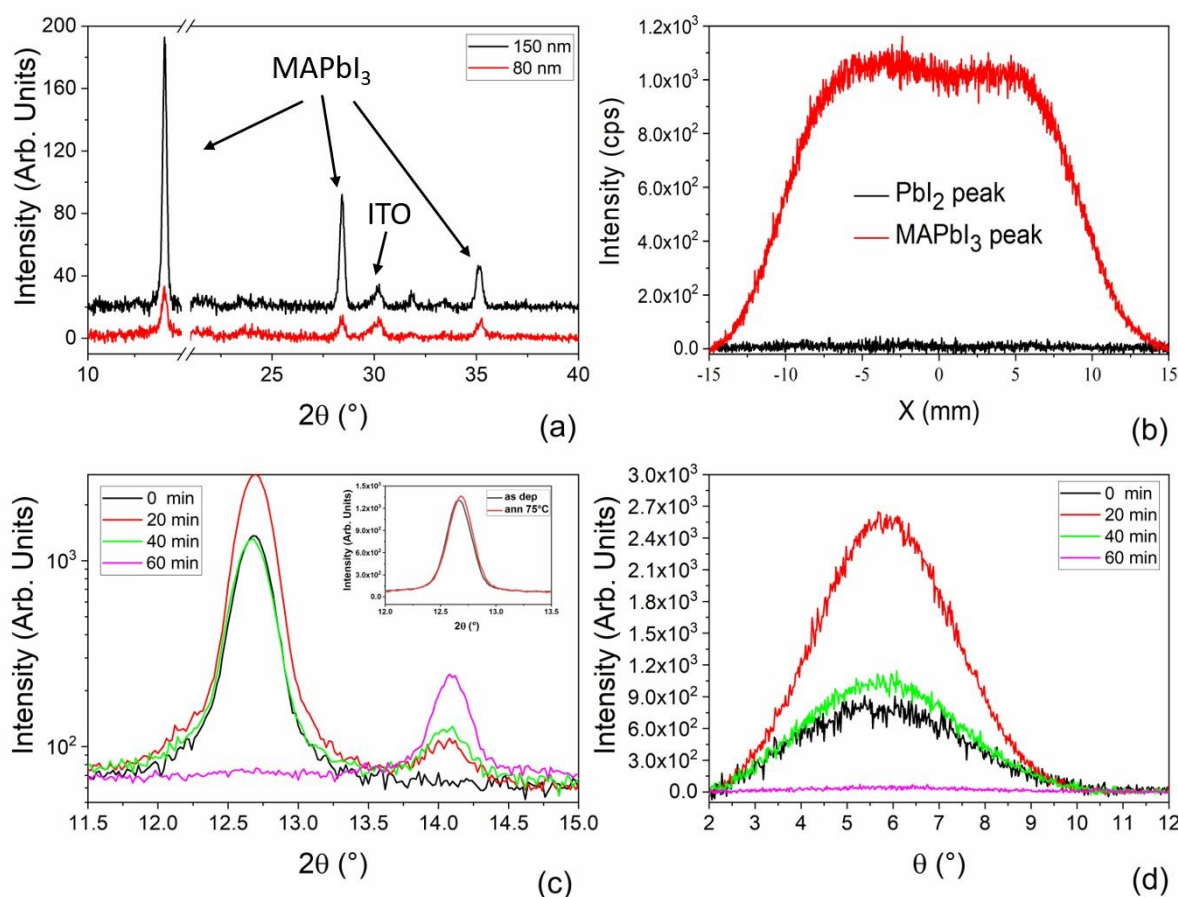
Figure 3 (a) Symmetric θ-2θ XRD patterns collected on MAPbI$_3$ layers with different thicknesses deposited on ITO/PTAA . (b) Integrated XRD spatial analyses along the X-axis collected at fixed 2θ angles of 14.10° (red curve) and 12.67° (black curve) in a 2.5cmx2.5 cm MAPbI$_3$ sample deposited on glass substrate (c) XRD patterns collected on deposited samples at different MAI time step on ITO/PTAA substrates. In the inset, the XRD patterns of as deposited PbI$_2$ sample and after a test annealing at 75 °C for 20 minutes. (d) Rocking curve collected at a fixed 2θ angle of 12.67° for samples corresponding to different MAI times on ITO/PTAA substrates.

To explore the uniformity of the film over the deposited area, X-scan analyses were performed on a 2 cm x 2 cm sample made of 150 nm-thick MAPbI$_3$ layer deposited on glass substrate. In the X-scan, the beam moving along X has a size of 2cmx1mm and two diffraction angles were used, namely at 14.11° for the MAPbI$_3$ and 12.67° for the PbI$_2$ (Figure 3b). We notice that the intensity of the curve related to the MAPbI$_3$ is uniform along X (box-like shape of the curve), while the intensity related to the PbI$_2$ is everywhere comparable with the noise, proving the compositional and thickness uniformity of the LV-PSE deposited MAPbI$_3$ layer.
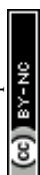
To study the MAPbI$_3$ formation kinetics via LV-PSE, we have deposited 85 nm of PbI$_2$ on ITO/PTAA and changed the duration of the second step of MAI evaporation. We used different progressively increasing deposition times, i.e. 20, 40 or 60 minutes, and correspondently we acquired the related diffraction patterns. In figure 3c we interestingly observe that after 20 minutes of MAI deposition the peak of the PbI$_2$ at 12.7° has a higher intensity than in the starting sample (PbI$_2$ only, t=0). Since the PbI$_2$ crucible is at room temperature during MAI deposition and indeed an addition of PbI$_2$ is excluded, this finding suggests that the initial molecular infiltration of Methylammonium Iodide inside the layer of PbI$_2$, with the related kinetic, improves the lattice order of the hosting material during the formation of the starting perovskite nuclei. To understand this phenomenon, we have added a post-deposition annealing step at 75 °C for 20 minutes with coupled in-situ XRD analysis to be confident that this rearrangement of the PbI$_2$ film is not simply caused by temperature. The test did not produce any increase of the PbI$_2$ diffracted peak as we would expect by a crystallization of the amorphous phase in the film after an annealing step. For further evaluation, we have additionally performed an annealing at 150 °C for 1h during X-ray diffraction analyses on a PbI$_2$ layer. In figure S1 the XRD patterns collected before and after the annealing do not show any significant increase of the peak intensity confirming that the layer is fully crystallized after deposition. We have also performed X-Ray Photoelectron Spectroscopy (XPS) analyses on the as deposited PbI$_2$ film to measure the atomic ratio between lead and iodine as well as to have information about the species inside the film (Fig.S3). Figure S3a shows the Pb4f spectral region with the typical lead doublet. After the deconvolution of the peaks, any sign of metallic lead is found but rather a doublet peak is detected with components centered at 138.60 eV (Pb4f$_{7/2}$) and 143.46 eV (Pb4f$_{5/2}$), typical of lead halides compounds. The absence of any Pb^0 is confirmed also by the quantitative analyses where a Pb/I ratio of 0.51 very close to the expected value is measured. We have acquired XPS spectra also after the 60 minutes of MAI deposition. The Pb/I ratio in this case is 0.35 that is also very close to the expected value of 0.33. In this case the Pb components are shifted at 136.20 eV (Pb4f$_{7/2}$) and 141.06 eV (Pb4f$_{5/2}$) due to the proximity of MA$^+$ cations.

To further investigate the observed rearrangement of the PbI$_2$ film during MAI deposition, rocking curves (rc) corresponding to the diagnostic peak at 12.67° were acquired. All the peaks reported in figure 3c denote a texturing of the PbI$_2$ layers along the [0001] direction. According to this, the rc peaks in figure 3d show that the highest degree of preferential orientation is promoted after 20 minutes of MAI deposition. After this first reorganization of the film, the peak intensity starts

decreasing due to the conversion of the PbI_2 into $MAPbI_3$. At the end of the process, we do not see PbI_2 left inside the film, thus confirming the complete material conversion.

To gain atomistic insights into the early mechanism of MAI diffusion within the PbI_2 lattice and their reaction, we performed DFT calculations, simulating the consecutive intercalation of MA^+/I^- complexes at the PbI_2 layers. Figure 4(a) shows the initial layered configuration of the PbI_2 crystal, where Pb atoms are aligned at the center of each layer, whereas I atoms are exposed at the layer surfaces. The initial diffusion of MAI molecular structures [Figures 3(b) and 3(c)] spontaneously triggers a reaction with the PbI_2 material, as the MA^+ cations interact through hydrogen bonding with I atoms of the PbI_2 crystal. As a result, this interaction weakens the PbI_2 bonds for Pb/I atoms that are adjacent to the MA^+ cations and favors the formation of novel Pb-I bonds between those Pb atoms and the iodide deriving from the MAI vapor. This process takes place through the displacement of the Pb atoms towards the interlayer area and consequently creates Pb voids within the PbI_2 layer. The Pb atoms that bind with the I atoms of the iodide vapor lose momentarily their octahedral coordination and acquire a 4-fold coordination, approaching the Pb^{4+} oxidation state. This condition is highly metastable, as the intercalation of further MA^+/I^- complexes gives rise to the construction of novel PbI_6 octahedra at the interlayer region (restoring the stable Pb^{2+} character of lead in iodide structures) and gradually transforms the two-dimensional PbI_2 layers into a three-dimensional structure [Figures 3(d) and 3(e)]. We expect that the kinetics of this process continue until the full transformation of the PbI_2 material into $MAPbI_3$.
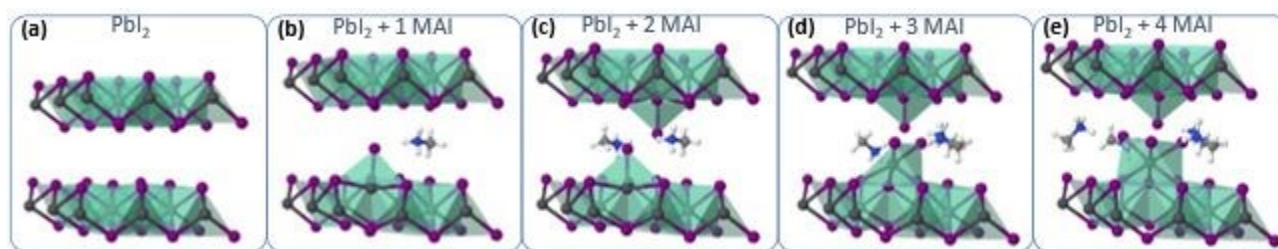

Figure 4 *DFT calculations of MAI intercalation within PbI_2 layers. (a) Ideal PbI_2 structure and intercalation of (b) 1 MAI molecule, (c) 2 MAI molecules, (d) 3 MAI molecules and (e) 4 MAI molecules within the layers of the PbI_2 structure.*

To deeply understand the time-dependent mechanism of MAI molecules incorporation into the PbI_2 pristine film, we have performed XRD analyses using grazing incidence geometries for all the samples prepared at various MAI step times. With this configuration, using different incidence angles, we can discriminate the mutual position of the PbI_2 and $MAPbI_3$ along the thickness of the film. In fact, lower is the incidence angle shallower is the portion of the layer contributing to the

signal. As can be seen in figure 6a the peak intensity at $2\theta=12.67°$ is higher for higher incidence angles according to that at 0.3° and 0.4° we are not able to investigate all the thickness. On the contrary at 0.5° we investigate the entire film thickness.

We want to point out that the XRD data reported in Figure 5 were acquired on the same samples reported in figure 3a and 3c but using a different acquisition geometry (grazing incidence configuration). Under grazing incidence, that is specifically useful for depth resolved analyses, the randomly oriented component of the films is detected whilst in symmetric $\theta-2\theta$ geometry (figure 3) the oriented (textured) part of the films contributes. Since it is demonstrated (polar figure in S2 and figure 3c) that the PbI_2 layer is highly textured, the random component is not as intense as the majority component taken in symmetric geometry. It is detected at relatively high incidence suggesting its location mostly at the bottom interface. On the other hand, as soon as the whole PbI_2 layer is converted to $MAPbI_3$ (figure 5d), no PbI_2 contribution is found whatever the incidence angle used.

The same behavior has occurred for all samples with the difference in the intensity that are more remarkable for the sample after 20 minutes of MAI (see figure 5b and decrease with time due to the consumption of PbI_2 during the formation of the perovskite. On the contrary the peaks at $2\theta=14.1°$ related to the $MAPbI_3$ film have the same intensity for the three incidence angles after the 20 minutes of MAI deposition. In this case, we investigate the upper portion of the layer suggesting that the first conversion of the PbI_2 to $MAPbI_3$ occurs at the top of the deposited PbI_2 film. After 40 minutes of MAI deposition, only the 0.3° incidence angle pattern show a slightly lower intensity for the $MAPbI_3$ peak with respect the 0.4° and 0.5° incidence angles. At 0.3° we are not able to collect the signal from all the already converted $MAPbI_3$ thickness, suggesting the increasing of the PbI_2 conversion to $MAPbI_3$ (figure 5c). Finally, in the sample after 60 minutes of MAI deposition (figure 5d) the signal related to the residual PbI_2 is not visible meaning that all the PbI_2 is converted into $MAPbI_3$ according with the lack of the PbI_2 peak shown in figure 3a. We additionally notice that the intensity of the $MAPbI_3$ peak at $2\theta=14.1°$ in figure 5d increases with increasing the incidence angle according to the progressively higher beam penetration depth. Based on our findings, we conclude that the conversion of the PbI_2 film to $MAPbI_3$ start from the topmost layer of PbI_2 progressively towards the lowermost part until the whole film is fully converted into $MAPbI_3$ as represented in figure 5e. This description agrees with previously reported works on PbI_2 conversion via gas-phase MAI deposition[56,57] thus framing the LV-PSE method as a solid-state reaction piloted by MAI diffusion.
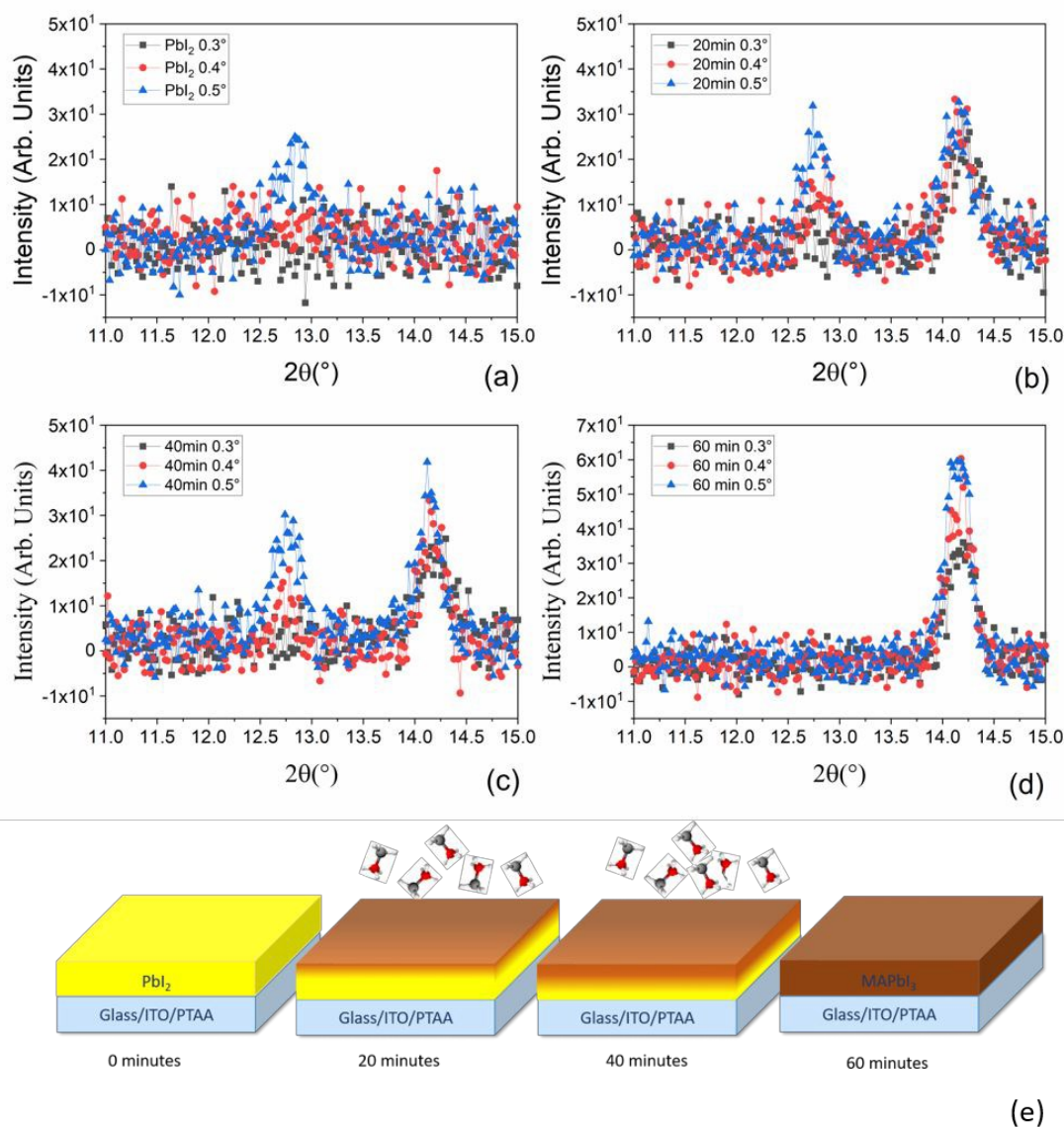
Figure 5 (a) XRD patterns collected in Grazing Incidence configuration at three different incidence angle, namely at 0.3°, 0.4° and 0.5° for PbI_2 deposited sample, (b) after 20 minutes, (c) 40 minutes and (d) 60 minutes of MAI deposition on ITO/PTAA substrates. (e) Schematic representation of the conversion mechanism from PbI_2 to $MAPbI_3$ during the MAI deposition step. In the pristine sample only the PbI_2 peak is detected at $2\theta=12.67°$. Along the MAI deposiiton step, the conversion of the PbI_2 to $MAPbI_3$ starts from the topmost part of the film toward the bottom until the complete conversion has occurred.

Morphological analyses

The process optimization done on the 150 nm thick $MAPbI_3$ layer has suggested a viable path for the downscaling on the perovskite layer thickness. On this basis, uniform and fully reacted layers that are only 80 nm-thick have been deposited by LV-PSE. The analyses of the morphology and of the optical properties of this very thin layer compared to the 150nm-thick $MAPbI_3$ film are hereafter discussed in detail.

Field emission scanning electron microscope (FE-SEM) analyses showed in figure 6 reveal a peculiar change in the morphologies of the films deposited during the LV-PSE processes. In figure 7a are

showed the images acquired after 15 minutes of PbI_2 deposition on an ITO/PTAA substrate used as template (first step) to grow the 80 nm thick $MAPbI_3$ film. The film is composed by randomly oriented PbI_2 small (around 100 nm) platelets-shaped grains. We have also performed chemical analyses on the 30 minutes deposited PbI_2 layer by Energy Dispersive X-ray (EDX) spectroscopy to check the composition (figure S4). The Pb/I ratio from EDX was 0.49 in good agreement with the expected value. The resulting $MAPbI_3$ film, after 30 minutes of MAI deposition, is compact with grain size around 100 nm. Most importantly, pinholes are not visible on the surface (figure 6b). According to what found in the thinner layer, the PbI_2 film deposited after 30 minutes (figure 6c) is also composed by platelets but with bigger size (200 nm). The comparison between the two samples demonstrate that the platelets continue to grow by proceeding PbI_2 deposition. The PbI_2 platelets are the template for the reacting $MAPbI_3$ film. As a matter of fact, the morphology of the $MAPbI_3$ is modelled on the PbI_2 platelets size, with final grain size similar to the one of the templating layers in both samples (figures 6 b and d). The incorporation of MAI into the PbI_2 platelets allows them to fill the empty space between the platelets due to the increase of cell volume during the conversion of the PbI_2 to $MAPbI_3$. The technologically interesting finding that such thin layers are totally compact without pinholes, in full agreement with XRD analysis in the X scan configuration, paves the way for extremely down-scaled PSCs.
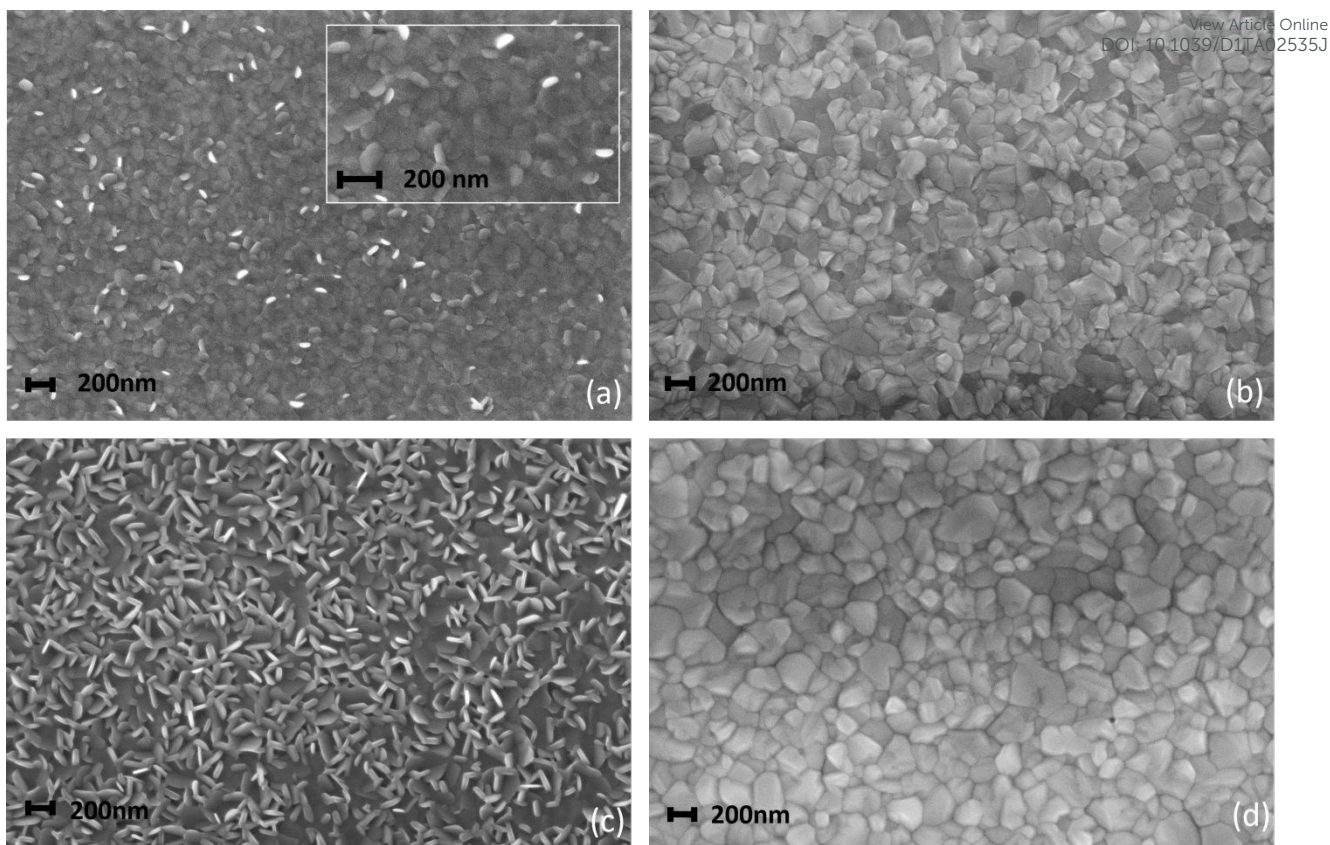
Figure 6 SEM images collected on (a) PbI₂ deposited on ITO/PTAA substrate using deposition time of 15 minutes and (b) the converted MAPbI₃ after 30 minutes of MAI deposition. (c) PbI₂ deposited for 30 minutes and (d) the resulted MAPbI₃ after 60 minutes of MAI deposition.

Optical properties

Transmittance spectra collected on both thick and thin samples deposited on ITO/PTAA substrates show the typical optical features of MAPbI₃ films (figure 7a) with an abrupt decrease below the gap (810 nm). The sample was kept in a closed chamber with an overpressure of N_2 to prevent degradation. The thickness of the perovskite layer (80 nm and 150 nm) was determined by verifying that n obeys the Cauchy equation in the transparent infrared region. The Average Visible Transmittance calculated for 150 nm and 80 nm samples in the range 400-800 nm were 20% and 32.8% respectively. Reducing the thickness of the active layer to 80 nm thus increases the transmittance in the visible range.
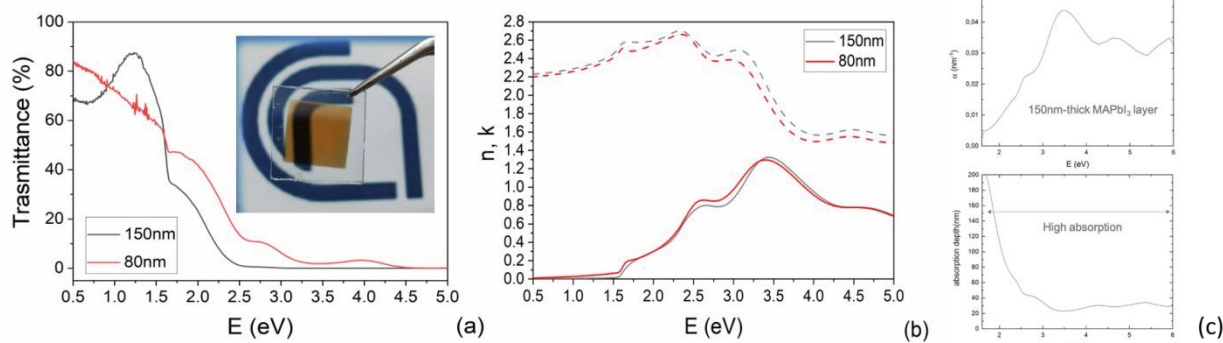
1
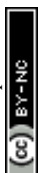
Figure 7 (a) Transmittances of 150 nm and 80 nm MAPbI$_3$ films. (b) The refractive index n (dashed line) and the extinction coefficient k (solid line) of 150 nm and 80 nm MAPbI$_3$ films. (c) absorption coefficient (nm^{-1}) and absorption depth (nm) of 150nm-thick MAPbI$_3$ layers.

In figure 7b we show the refractive index n and the extinction coefficient k, strictly related to the absorption coefficient of the material, extracted by Spectroscopic Ellipsometry (SE) measurements for the two PSK layers. The thickness of the perovskite layer (80 nm and 150 nm) was determined by verifying that n obeys the Cauchy equation in the transparent infrared region. The measurements were done on glass substrates to exclusively probe the absorbing layer. The sample was kept in a closed chamber with an overpressure of N$_2$ to prevent degradation. Interband transition have been identified by applying the critical points analysis.[58-60] Critical points (CPs) analyses is based on the simultaneous fit of the second derivatives of the real and imaginary part of the dielectric function (ε) with a function like (one for each CP):

$$\frac{\partial^2 \varepsilon}{\partial \omega^2} = n(n-1)Ae^{i\Phi}(\omega - E + i\Gamma)^{(n-2)} \qquad \text{eq 4}$$

where A, Φ, E, Γ and n are the amplitude, phase, energy position, broadening and the dimensionality of the CP. The similarity of the critical points positions (see Table 1) denotes that the LV-PSE process allows downscaling the MAPbI$_3$ thickness while preserving the material band structure.

Table 1 Energy band gap and critical point values extracted by the critical point analyses performed onspectroscopic ellipsometry data.

	Eg (eV)	E1 (eV)	E2 (eV)	E3 (eV)
THIN	1.612±0.001	2.505±0.003	3.21±0.01	4.52±0.06
THICK	1.605±0.001	2.423±0.008	3.28±0.02	4.27±0.18

In figure S5 are reported the ellipsometric experimental data (Psi and Delta) collected at various angles and the Cauchy fit. In addition to this, the absorption coefficient was measured by Spectroscopic Ellipsometry and converted into absorption depth as a function of the incident photon energy as shown in figure 7c for the 150 nm-thick layer. The combination of the two parameters highlights that, even in a relatively thin layer, the absorption capability is still high above the bandgap. As a matter of fact, ~60% of incident photons with energy above 2 eV are absorbed within the first 20-100 nm in the $MAPbI_3$ layer. Photons with energy in the range of energy 1.5-2 eV are absorbed within 100-200 nm with indeed only a partial loss of absorption that, on the other hand, guarantees the semitransparency of the layer without excessively penalizing the devices performances.

In order to evaluate material quality, we recorded the steady state photoluminescence, we measured its quantum yield (PLQY) and we analyzed the PL decay (TRPL) of as-deposited pristine isolated 150 nm $MAPbI_3$ films deposited on glass substrates (figure 8). The PLQY determined on a non-quenching substrate is used to estimate the maximum value of the material-specific luminescence yield. This quantity is a direct measure for the optoelectronic quality of the absorber material, as a low emission yield means high additional non-radiative recombination, which would not allow for high Voc.[61,62] The PLQY, in turn, strongly depends upon the excitation fluences, as high densities of carriers would passivate active defect raising radiative channels.
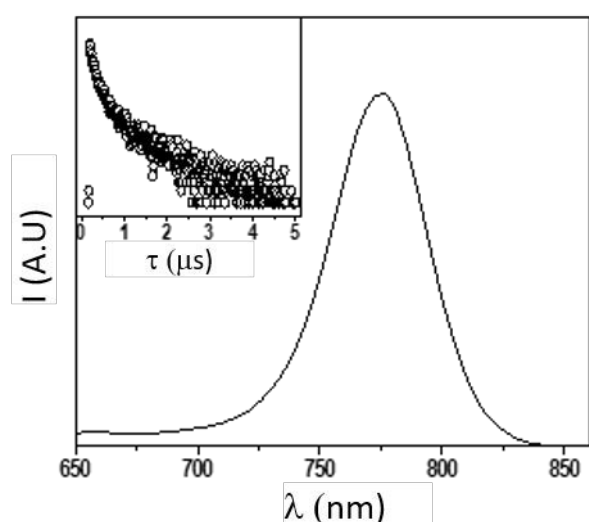

Figure 8 Emission spectrum (main, exc = 405 nm) and corresponding lifetime decay (inset, exc = 405 nm; em: 750 nm) of $MAPbI_3$ thin film on glass.

At very low excitation fluency (< 1.0 $mWcm^{-2}$), only few reports on $MAPbI_3$ show PLQY around 1 % and those are associated to post treated samples or chloride including samples[63] here we record a

0.9 % PLQY using 0.6 mWcm^{-2} power excitation fluences, implying an optimal thin film for photovoltaic exploitation. An additional evidence of this claim is suggested by time resolved PL analyses, which show long living free carriers. In line with what usually observed for hybrid organic-inorganic perovskites, we found a complex exponential decay (in this case a biexponential function best fits the decays), since there is no clear consensus on how to exactly assign the various components to a given TRPL curve, we used a weighted average of the diverse decay components:

$$\frac{\alpha_1 \tau_1^2 + \alpha_2 \tau_2^2}{\alpha_1 \tau_1 + \alpha_2 \tau_2} \qquad \text{eq 5}$$

obtaining a value of 234 ns.[63] This is a very long radiative decay for pristine MAPbI$_3$[63] considering that lifetimes in the order of μs have been observed only when chloride anions were added to the precursor's solutions, with a beneficial role played by these ions in the growth of large crystallites. These results imply that LV-PSE is an optimal technique for the deposition of thin perovskite performing layers.

Electrical properties

In the light of all our findings, the two MAPbI$_3$ thin layers have been implemented in the p-i-n PSC architectures and tested. The efficiency values recorded on the two set of PSCs as a function of the MAPbI$_3$ thickness testifies outstanding performances not yet reported in the literature for such thin layers. In addition, it is worth of note a full lack of hysteresis during forward and reverse scans as shown in figure 9, due to the use of the organic ETL and HTL materials but also ascribed to the high quality of the perovskite film[64-66]according to PL and SE analyses.
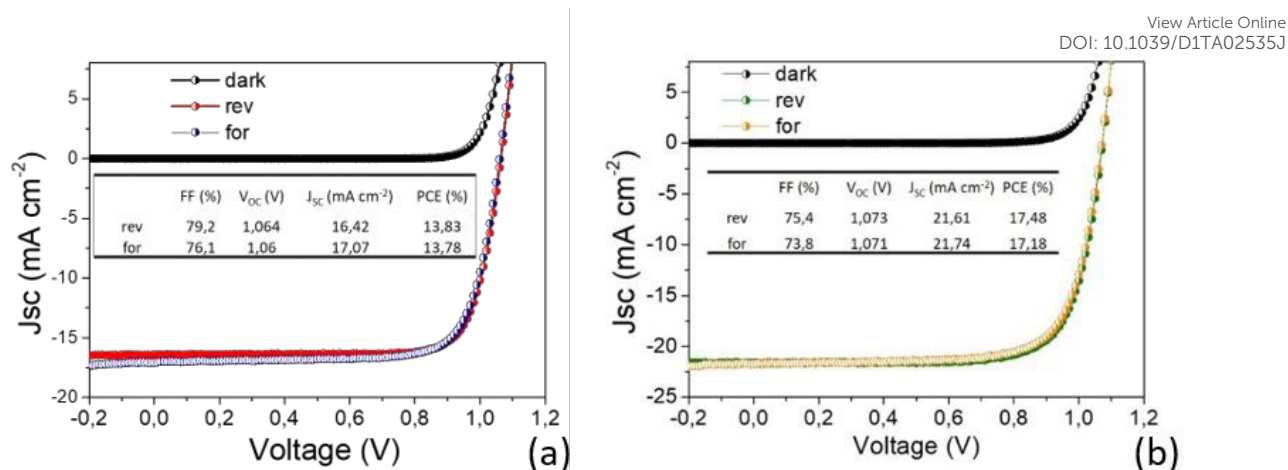
Figure 9 I-V characterization of the best prepared devices with (a) 80 nm and (b) 150 nm MAPbI$_3$ active layer. The AVT moves from 32.8%. to 20%
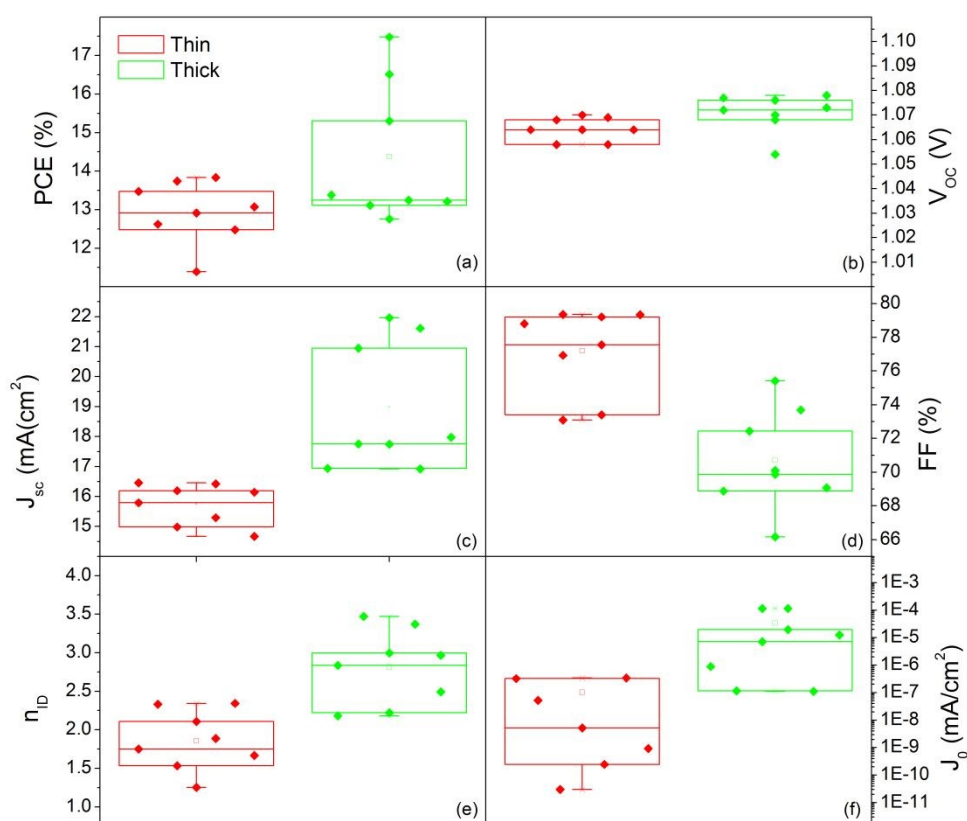

Figure 10 Box plot of (a) efficiency (PCE), (b) open circuit voltage (V$_{oc}$), (c) short circuit current (J$_{sc}$), (d) fill factor (FF), ideality factor (n$_{iD}$) and (f) reverse saturation current (J$_0$) from electrical characterization of all prepared devices with 80 nm thick and 150 nm thick MAPbI$_3$ active layer

Figure 10 shows the distribution of photovoltaic parameters displayed as boxplots for 16 cells fabricated with 80 nm (8 cells) and 150 nm (8 cells) MAPbI$_3$ layer. The average value of power conversion efficiency (PCE) for the two set of devices is 12.9% and 14.4%, respectively. The best

fabricated device exhibits a 17.48% efficiency (MAPbI$_3$ 150 nm-thick) that stabilizes at 16.5% upon light soaking, (figure S6). The record for 80 nm-thick layers instead is 13.8%, with a narrow distribution of the other measured values. These results place our devices among the best semitransparent devices based on MAPbI$_3$[67,68] and further show how this deposition protocol represent an important progress in the field.

Small differences in the open circuit voltage (V$_{oc}$) values, in the range 1.05 -1.08 V (figure 10b), are found between the two families of devices, whilst the short circuit current (J$_{sc}$) is definitely higher in the thicker devices (figure 10c). The Fill Factor (FF) has instead a countertrend with the device thickness (77% vs 71%) that can account for different shunt or series resistances (figure 10d). To add some insights on that, we additionally provide the statistical distributions of ideality factor (n$_{ID}$) and reverse saturation current (J$_0$) in figure 10e and 10f respectively, calculated according to ref[69] using the eq S1 and S2. The ideality factor was also differently calculated following Tress et al.[70] using the J-V curve taken in dark condition with results confirming the gap vs. MAPbI$_3$ thickness.

The lower values of n$_{ID}$ in thin devices can indicate a better heterojunction quality[70]. The relationship is not necessarily straightforward[70,71] , but, in this respect, we additionally notice that low n$_{ID}$ corresponds to low J$_0$. This statistical evidence, complemented with the higher FF, indeed denotes a lower non-radiative recombination in the thin PSC likely associated to a less pronounced interfacial trapping.[72,73] The thickness halving without proportionally reducing the efficiency satisfies the technological requirements for transparent PSC, and represents a unique example in the current panorama of similar deposition method.[24,36]

4. Conclusions

We described a newly designed two-step vacuum deposition process called LV-PSE to prepare high quality MAPbI$_3$. The process benefits from the low vacuum condition and the short diffusion path (~2 cm) of the sublimated species that provides high pressure and high temperature to the sublimated species reaching the substrate side. This unique configuration allows controlling the rate of mass exchange at the vapor-substrate interface for a fine tuning of the material quality.

We disclose that the conversion of the PbI$_2$ film to MAPbI$_3$ starts from the top-surface of the film to the bulk via an adsorption-incorporation-migration mechanism guided by the gradient of MAI concentration. The final MAPbI$_3$ layer is composed by grains with a diameter from 50 to 200 nm. The film is compact and without pinhole that makes the perovskite suitable for photovoltaic

application. The PL analyses, according to SE, showed that the active layer has very low tail of electronically active defects, and indeed, on this basis, we were able to build up efficient solar cell with p-i-n architecture. With just 80 nm-thick active layers we achieved a mean efficiency value of 12.9% and best value of 13.8% with an AVT value of 32.8% that makes these devices unique in the current panorama of MAPbI$_3$ materials prepared with different methods and suitable for the application in BIPV. Using 150 nm-thick films we were able to achieve 14.4% mean efficiency and a best stabilized efficiency value of 16.5% with no hysteresis ascribed to low density of defects inside the layer and at the interfaces coupled with organic ETL and HTL. To our knowledge, this value represents the highest efficiency published on p-i-n architecture for similar scaled thicknesses.

The use of LV-PSE and the scaled MAPbI$_3$ thicknesses, associated with excellent efficiency values, paves the way for an affordable cost reduction for devices fabrication besides allowing a reduction by ~1/3 of the Pb content inside the devices against environmental concerns.

Conflicts of interest

There are no conflicts to declare.

Acknowledgment

References

1   J. Burschka, N. Pellet, S.-J. Moon, R. Humphry-Baker, P. Gao, M. K. Nazeeruddin and M. Grätzel, *Nature*, 2013, **499,** 316–9.

2   N. J. Jeon, J. H. Noh, W. S. Yang, Y. C. Kim, S. Ryu, J. Seo and S. Il Seok, *Nature*, 2015, **517**, 476–480.

3   A. K. Jena, A. Kulkarni, and T. Miyasaka,*Chem. Rev.,* 2019, **119**, 3036-3103

4   W. Huang, J. S. Manser, P. V. Kamat and S. Ptasinska, *Chem. Mater.*, 2016, **28, 1**, 303–311.

5   M. Zhang, F. Yuan, W. Zhao, B. Jiao, C. Ran, W. Zhang and Z. Wu, *Org. Electron. Physics, Mater. Appl.,* 2018, **60**, 57–63.

6   V. Adinolfi, W. Peng, G. Walters, O. M. Bakr and E. H. Sargent, *Adv. Mater.,* 2018, **30**, 1–13.

7   J. Zhou and J. Huang, *Adv. Sci.*, 2018, **5**. 1700256

8   N. Patel, S. Dias and S. B. Krupanidhi, *J. Electron. Mater.*, 2018, **47,** 2306–2315

9   H. W. Chen, N. Sakai, A. K. Jena, Y. Sanehira, M. Ikegami, K.-C. Ho and T. Miyasaka, *J. Phys. Chem. Lett.,* 2015, **6,** 1773–1779

10   S. D. Stranks, G. E. Eperon, G. Grancini, C. Menelaou, M. J. P. Alcocer, T. Leijtens, L. M. Herz, A. Petrozza and H. J. Snaith, *Science,* 2013, **342**, 341–344

11   https://www.nrel.gov/pv/assets/pdfs/best-research-cell-efficiencies.20201228.pdf

12   A. Kojima, K. Teshima, Y. Shirai and T. Miyasaka*, J. Am. Chem. Soc.*, 2009, **131**, 6050–1

13   Y. Zhao and K. Zhu, *J. Phys. Chem. Lett.*, 2014, **5**, 4175–4186.

14   W. S. Yang, J. H. Noh, N. J. Jeon, Y. C. Kim, S. Ryu, J. Seo and S. Il Seok, *Science,* 2015, **348**,1234-1237

15   A. Ng, Z. Ren, Q. Shen, S. H. Cheung, H. C. Gokkaya, S. K. So, A. B. Djurišić, Y. Wan, X. Wu and C. Surya, *ACS Appl. Mater. Interfaces, 2016*, **8**, 32805–32814

16   E. Smecca, Y. Numata, I. Deretzis, G. Pellegrino, S. Boninelli, T. Miyasaka, A. La Magna and A. Alberti, *Phys. Chem. Chem. Phys.* 2016, **18**,13413–13422.

17   I. Deretzis, E. Smecca, G. Mannino, A. La Magna, T. Miyasakaand A. Alberti, *J. Phys. Chem. Lett.* 2018*,* **9,** 3000 −3007.

18   A. Alberti, I. Deretzis, G. Mannino, E. Smecca, F. Giannazzo, A. Listorti, S. Colella, S. Masi and A. La Magna, *Adv.Energy Mater.* 2019, **9**, 1803450.

19   A. J. Knight and Laura M. Herz, *Energy Environ. Sci.*, 2020, **13**,202

20   I. Deretzis, A. Alberti, G. Pellegrino, E. Smecca, F. Giannazzo, N. Sakai, T. Miyasaka and A. La Magna, *Appl. Phys. Lett.* 2015, **106**, 131904.

21   M. Liu, M. B. Johnston and H. J. Snaith, Nature, 2013, **501**, 395–398.

22   W. A. Dunlap-Shohl, E. T. Barraza, A. Barrette, K. Gundogdu, A. D. Stiff-Roberts and D. B. Mitzi, *ACS Energy Letters,* 2018, **3 (2),** 270-275

23   N. J. Jeon, J. H. Noh, W. S. Yang, Y. C. Kim, S. Ryu, J. Seo and S. Il Seok, *Nature,* 2015, **517,** 476–480

24   B. Danekamp, N. Droseros, F. Palazon, M. Sessolo, N. Banerji and H. J. Bolink. *ACS Appl. Mater. Interfaces* 2018, **10**, 36187–36193.

25   D. Perez-Del-Rey, P. P. Boix, M. Sessolo, A. Hadipour, H. J. Bolink, *J. Phys. Chem. Lett.* 2018, **9**, 1041.

26   V. Arivazhagan, J. Xie, Z. Yang, P. Hang, M. M. Parvathi K. Xiao, C. Cui, D. Yang and X. Yu, *Solar Energy*, 2019, **181**,339–344

27   Q. Guo, C. Li, W. Qiao, S. Ma, F. Wang, B. Zhang, L. Hu,S. Dai and Z. Tan, *Energy Environ. Sci.,*2016, **9**, 1486

28   L. Gu, S. Wang, X. Fang, D. Liu, Y. Xu, N. Yuan and J. Ding. *ACS Appl. Mater. Interfaces* 2020, **12**, 33870–33878

29   A. Ng, Z. Ren, Q. Shen, S. H. Cheung, H. C. Gokkaya, G. Bai, J. Wang, L. Yang, S. K. So, A. B. Djurišić, W. W. Leung, J. Hao, W. K. Chan and C. Surya, *J. Mater. Chem.* A, 2015,**3**, 9223-9231

30   M. J. Bækbo, O. Hansen, I. Chorkendorff and P. C. K. Vesborg, *RSC Adv.,* 2018, **8**, 29899

31   Z. Zhou, Z. Qiang, T. Sakamaki, I. Takei, R. Shang and E. Nakamura. ACS *Appl. Mater. Interfaces* 2019, **11**, 22603−22611

32   A. Cannavale, P. Cossari, G. E. Eperon, S. Colella, F. Fiorito, G. Gigli, H. J. Snaith and A. Listorti. *Energy Environ. Sci.,* 2016, **9**, 2682-2719

33   C. Roldan-Carmona, O. Malinkiewicz, R. Betancur, G. Longo, C. Momblona, F. Jaramillo, L. Camacho and H. J. Bolink, *Energy Environ. Sci.,* 2014, **7**, 2968–2973.

34   J. H. Lee, J. H. Heo, S. H. Im and O. O. Park. *ACS Applied Materials & Interfaces* 2020, **12 (9),** 10527-10534

35   G. E. Eperon, V. M. Burlakov, A. Goriely and H. J. Snaith, *ACS Nano,* 2014,**8**, 591–598.

36   H. Wang, H. A. Dewi, T. M. Koh, A. Bruno, S. Mhaisalkar and N. Mathews, *ACS App. Mater. & Interf.* 2020, **12**, 484-493

37   C.-Y. Chang, K.-T. Lee, W.-K. Huang, H.-Y. Siao and Y.-C. Chang, Chem. Mater., 2015, 27, 7119.

38   J. H. Heo, H. J. Han, M. Lee, M. Song, D. H. Kim and S. H. Im, *Energy Environ. Sci.,* 2015, **8**, 2922–2927.

39   Z. Li, Y. Zhao, X. Wang, Y. Sun, Z. Zhao, Y. Li, H. Zhou and Q. Chen, *Joule* 2018, **2**, 1559–1572

40   H. Shen, T. Duong, J. Peng, D. Jacobs, N. Wu, J. Gong, Y. Wu, S. K. Karuturi, X. Fu, K. Weber, X. Xiao, T. P. Whitead K. Catchpole *Energy Environ. Sci*.,2018,**11**,394

41   J. Xu, C. C. Boyd, Z. J. Yu, A. F. Palmstrom, D. J. Witter, B. W. Larson, R. M. France, J. Werner, S. P. Harvey, E. J. Wolf, W. Weigand, S. Manzoor, M. F. A. M. van Hest, J. J. Berry, J. M. Luther, Z. C. Holman and M. D. McGehee *Science* 2020, **367**, 1097–1104

42   L. K. Ono, S. Wang, Y. Kato, S. R. Raga, Y. Qi. *Energy Environ. Sci.,* 2014, **7**,3989

43   Patent pending

44   S. Masi, F. Aiello, A. Listorti, F. Balzano, D. Altamura, C. Giannini, R. Caliandro, G. Uccello-Barretta, A Rizzo and S. Colella . *Chem. Sci***,** 2018,**9**, 3200-3208

45   Giannozzi, P.; Baroni, S.; Bonini, N.; Calandra, M.; Car, R.; Cavazzoni, C.; Ceresoli, D.; Chiarotti, G. L.; Cococcioni, M.; Dabo, I. et al.. *Journal of physics: Condensed matter* 2009, **21**, 395502.

46   J. P. Perdew, K. Burke and M. Ernzerhof, *Phys. Rev. Lett.* 1996, **77**, 3865.

47   D. Vanderbilt, *Phys. Rev. B* 1990, **41**, 7892.

48   H. J. Monkhorst and J. D. Pack, *Phys. Rev. B* 1976, **13**, 5188.

49   S. Hsiao , H. Lin , W. Lee , W. Tsai , K. Chiang ,W. Liao , C. Ren-Wu , C. Chen and H. Lin, *Adv. Mater. 2016*, **28**, 7013–7019

50   R. Kendler, F. Dreisbach, R. Seif, S. Pollak. and M. Petermann, , *Rev. Sci. Instrum.* ,2019, **90**, 055105

51   D.D. Avrov, A.S. Bakin, S.I. Dorozhkin, V.P. Rastegaev, Y.M. Tairov, *Journal of Crystal Growth,* 1999, **198-199** 1011—1014

52   J. S. Chickos and W. E. Acree Jr., *J. Phys. Chem. Ref. Data Vol 2,* , 2002, **31**, 537–698

53   A. Dualeh, P. Gao, S. Il Seok, M. K. Nazeeruddin and M. Gratzel, *Chem. Mater.* 2014, **26**, 6160–6164

54   A. Alberti, I. Deretzis, G. Pellegrino, C. Bongiorno, E. Smecca, G. Mannino, F. Giannazzo, G. G. Condorelli, N. Sakai, T. Miyasaka, C. Spinella and A. La Magna, *Chem. Phys. Chem.,* 2015, **16**, 3064.

55   A. Alberti, E. Smecca, S. Sanzaro, G. Mannino, I. Deretzis and A. La Magna, *Riv. del Nuovo Cim*. 2019, **42**, 301–366.

56   S. Ngqoloda, C. J. Arendse, T. F. Muller, P. F. Miceli, S. Guha, L. Mostert and C. J. Oliphant. *ACS Appl. Energy Mater*. 2020, **3**, 2350–2359

57   H. Xu, F. Xu, W. Wang, Y. Zhu, Z. Fang, B. Yao, F. Hong, J. Cui, F. Xu, R. Xu, C. Chen and L. Wang, *Organic Electronics,* 2019, **69,** 329–335

58   G. Mannino, A. Alberti, I. Deretzis, E. Smecca, S. Sanzaro, Y. Numata, T. Miyasaka, and A. La Magna, *J. Phys. Chem. C,* 2017, **121**, 7703–7710

59   G. Mannino, I. Deretzis, E. Smecca, A. La Magna, A. Alberti, D. Ceratti and D. Cahen, *J. Phys. Chem. Lett.,* 2020, **11,** 2490–2496

60   A. Alberti, I. Deretzis, G. Mannino, E. Smecca, S. Sanzaro, Y. Numata,T. Miyasaka and A. La Magna, *J. Phys. Chem. C,* 2017, **121**, 13577–13585

61   W. Tress N. Marinova O. Inganäs, M. K. Nazeeruddin, S. M. Zakeeruddin and M. Graetzel, *Adv. Energy Mater*., 2015, **5**, 1400812

62   K. Tvingstedt, O. Malinkiewicz, A. Baumann, C. Deibel, H. J. Snaith, V. Dyakonov and H. J. Bolink, *Scientific Reports* 2014, **4**, 6071

63   J. R. Lakowicz, Principles of Fluorescence Spectroscopy, Springer, New York, 2006

64   V. Trifiletti, N. Manfredi, A. Listorti, D. Altamura, C. Giannini, S. Colella, G. Gigli and A. Rizzo, *Adv. Mater. Inter.,* 2016, **3 (22),** 1600493

65   T. Pang, K. Sun, Y. Wang, S. Luan, Y. Zhang, Y. Zhu, Z. Hu and R. Jia, *J. Mater. Chem. C,* 2020,**8,** 1962

66   C. Tong, L. Li, L. Liu and O. V. Prezhdo, *J. Am. Chem. Soc.* 2020, **142**, 3060–3068

67   W. E. I. Sha, X. Ren, L. Chen and W. C. H. Choy, *App. Phys. Lett.,* 2015, **106**, 221104

68   L. Yuan, Z. Wang, R. Duan, P. Huang, K. Zhang, Q. Chen, N. K. Allam, Y. Zhou, B. Song and Y. Li *J. Mater. Chem. A,* 2018, **6,** 19696

69   P. Liao, X. Zhao, G. Li, Y. Shen and M. Wang, *Nano-Micro Lett*., 2018, **10**, 5

70   W. Tress, M. Yavari, K. Domanski, P. Yadav, B. Niesen, J. P. Correa Baena, A. Hagfeldt and M. Graetzel, *Energy Environ. Sci,* 2018, **11**, 151

71   P. Caprioglio, C. M. Wolff, O. J. Sandberg, A. Armin, B. Rech, S. Albrecht, D. Neher and M. Stolterfoht, *Adv. Energy Mater.* 2020, **10**, 2000502

72   D. Moia, I. Gelmetti, P. Calado, W. Fisher, M. Stringer, O. Game, Y. Hu, P. Docampo, D. Lidzey, E. Palomares, J. Nelson and P. R. F. Barnes, *Energy Environ. Sci.,* 2019, **12**, 1296.

73   I. Zarazua, G. Han, P. P. Boix, S. Mhaisalkar, F. Fabregat-Santiago, I. Mora-Seró, J. Bisquert and G. Garcia-Belmonte, *J. Phys. Chem. Lett. 2016*, **7**, 5105–5113